Design, Manufacturing and Quality Assessment of 3D-Printed Anthropomorphic Breast Phantom for Mammography

Elma Huseljić[1], Senad Odžak[1], Adnan Beganović[1,2(✉)], Almasa Odžak[1], Adi Pandžić[3], and Merim Jusufbegović[2]

[1] Faculty of Science, University of Sarajevo, Zmaja od Bosne 33-35, 71000 Sarajevo, Bosnia and Herzegovina
{senad.odzak,adnan.beganovic,almasa.odzak}@pmf.unsa.ba
[2] Clinical Center of the University of Sarajevo, Bolnička 25, 71000 Sarajevo, Bosnia and Herzegovina
merim.jusufbegovic@fzs.unsa.ba
[3] Faculty of Mechanical Engineering, University of Sarajevo, Vilsonovo šetalište 9, 71000 Sarajevo, Bosnia and Herzegovina

Abstract. Radiological anthropomorphic phantoms are objects that mimic patient's anatomy when imaged by x-rays. These objects play a major role in optimizing radiation dose and image quality, allowing repeated exposure without exposing patients to harmful ionizing radiation. The goal of this study was to create a three-dimensionally-printed (3D-printed) phantom that would allow production of images that closely match those of human breast produced in digital mammography. We determined the attenuation properties of the Gray V4 resin using an imaged step-wedge. Gray values in image were associated with corresponding material thickness and a real mammogram was converted to two-dimensional (2D) matrix with elements whose values correspond to material thickness. Geometrical corrections for perspective and projection were taken into account. A standard triangle language (STL) file was used as input for the 3D printer. The quality of the printed phantom was evaluated by comparing its images to those of the real patient mammogram using different quantifying measures in spatial and frequency domain. The calculated similarity index (SSIM) was approximately 0.99, which indicates that SLA 3D printing technology can be successfully utilized to produce mammography phantoms.

Keywords: 3D printing · Mammography · Phantom · Image similarity

1 Introduction

Mammography is the most commonly used imaging modality in clinical practice for screening women for breast abnormalities and is a key tool for the early detection of breast cancer. Physical phantoms are commonly used as surrogates for breast tissue to evaluate the performance of mammography systems [1–4]. Recent advances in technology, such

A. Badnjević and L. Gurbeta Pokvić (Eds.): MEDICON 2023/CMBEBIH 2023, IFMBE Proceedings 93, pp. 221–231, 2024.
https://doi.org/10.1007/978-3-031-49062-0_24

as 3D printing, have enabled the development of complex, anatomically realistic breast phantoms that have the potential to improve the evaluation of mammography systems [5].

In this study, we developed a reproducible method for creating breast phantoms using 3D printing technology. To achieve this, we developed custom software in MATLAB that takes a standard DICOM 2D mammography image as input and produces a 3D triangle mesh object as output that represents the observed attenuation of the original breast. The generated triangle mesh is stored in a generic format, which can be easily converted to the popular standard triangulation or standard tessellation language format (STL) used by most printers. The gray level of each pixel in the mammography image provides information about the radiological thickness of the breast in the direction from the focal point of the x-ray source to the pixel [6]. By taking into account the differences in x-ray attenuation between the breast tissue and 3D printing material, the observed radiological thickness in pixels can be converted to the thickness of the printed material that will produce an equivalent amount of x-ray attenuation. This process allows for the creation of an anatomically realistic breast phantom that accurately represents the x-ray attenuation properties of actual breast tissue [7].

After the realization of the phantom, its success was tested, analyzing the quality of the original clinical image and the created phantom image. Image quality is often characterized by well-known measures and criteria, usually related to radiometry, such as contrast, brightness, noise variance, and radiometric resolution. Image sharpness is a key indicator when measuring image quality [8].

2 Material and Methods

2.1 Clinical Mammography System

Full-field digital mammography (FFDM) is an advanced imaging technology that offers high accuracy and precision in detecting breast cancer. Compared to traditional film mammography, FFDM provides greater clarity and detail in breast images, making it easier for radiologists to identify potential abnormalities. The use of FFDM has been shown to reduce the need for follow-up diagnostic procedures, as well as the number of false positives and unnecessary biopsies.

In FFDM, pixel values represent the amount of x-ray radiation that has been absorbed by the breast tissue at each point in the image. These values are measured in units of grayscale and are used to create a detailed image of the breast. Areas of the breast that absorb more x-rays, such as denser tissues like tumors, will appear as brighter or whiter on the image, while areas that absorb fewer x-rays, such as fatty tissue, will appear darker or blacker on the image.

DICOM (Digital Imaging and Communications in Medicine) is a standard format for medical images that include both the image data and the associated metadata. DICOM images can be classified into two main categories: “for processing” (raw) and “for presentation.” Raw images are acquired from the imaging equipment before any processing or analysis is performed. These images contain all the information captured by the imaging equipment and are typically stored in a lossless format to preserve image quality. In raw DICOM images, the pixel value is directly correlated to the air kerma received by

the detector ($K_{i,d}$) during the imaging process. The relationship between the pixel value and the dose of radiation is usually linear and can be used to calculate the radiation dose at any point in the image using a calibration curve.

In mammography, the x-ray source is typically located above the breast, while the detector is located below. The breast is compressed between these two plates to ensure uniform thickness and reduce motion artifacts. The x-ray beam is collimated to minimize scatter radiation and to ensure that only the breast tissue is imaged. The x-ray beam used in mammography is typically a low-energy beam, which allows for better visualization of the breast tissue. The x-rays are absorbed differently by different types of breast tissue, such as dense or fatty tissue, allowing for the detection of abnormalities. The source-to-detector distance (f), is an important parameter in medical imaging that affects the quality of the image obtained. In general, f refers to the distance between the x-ray source (focal spot) and the detector used to capture the x-ray image.

In this study, Hologic Selenia Dimensions digital mammography system was used to obtain craniocaudal (CC) images during patient and phantom imaging. The patient had undergone a regular examination using the following exposure parameters: tube voltage (U) of 29.0 kV and tube current-exposure time product (Q) of 126.0 mA s, both determined by automatic exposure control (AEC). The associated compression force was 58.4 N. The phantom, however, was exposed using $U = 29.0$ kV and $Q = 120$ mA s, selected manually, with no compression. The source-to-detector distance (f) is the same in both cases.

2.2 Characterization of the Material Used in 3D Printing

The surface of the 3D-printed phantom is defined by the material and the printing technique [9]. In this work, a phantom sample was printed using a stereolithography (SLA) printer that uses stereolithography technology and prints using liquid resin polymerized with an ultraviolet laser. The breast phantom was 3D printed with Grey V4 (Formlabs, Somerville, MA, USA), a material most commonly used for high-resolution rapid prototyping, product development, and design. Grey V4 is intended for the SLA printing of models with precise details; it has a matte finish and opaque appearance [10].

The surface of this material is very smooth. It is rigid, with medium mechanical resistance. Design freedom is limited due to the structure needed to support the model during printing. Unlike transparent resin, which is also used in SLA printing, the gray resin is excellent at showing details [11].

2.3 Phantom Design

The design of the phantom relied on a real CC mammogram with visible adipose and glandular tissue, with regions containing microcalcifications and other commonly visible objects. Their visibility relies on differences in x-ray attenuation caused by different density and atomic composition. This attenuation pattern can be simulated using an object made of a homogeneous material that changes its thickness accordingly. This process consists of three steps.

The first step consisted of determining the attenuation properties of Grey V4 resin. A step-wedge was printed and imaged using the mammography unit. Gray values in

the raw and unprocessed mammography image were associated with the corresponding material thickness. Data was fitted using the following regression curve (Fig. 1):

$$f(z) = \left(\frac{z-c}{a}\right)^{\frac{1}{b}}, \tag{1}$$

where the fitting parameters have values of $a = 290.1 \pm 4.5$, $b = -0.149 \pm 0.014$, $c = -72.2 \pm 8.5$ ($R^2 = 0.999$). Figure 1 demonstrates small differences between values of a fitted curve (blue curve) and measured data (red points). This is also visible in the region of thicker material, which is shown in a zoomed-in view of this area.

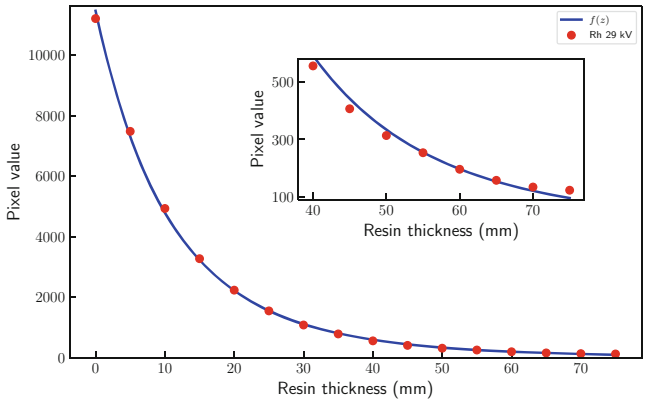

Fig. 1. Thickness of Grey V4 resin corresponding to different pixel values in raw full-field digital mammography image. The regression curve is in form of $p = \left(\frac{z-c}{a}\right)^{\frac{1}{b}}$, ($a = 290.1 \pm 4.5$, $b = -0.149 \pm 0.014$, $c = -72.2 \pm 8.5$, $R^2 = 0.999$).

In the second step, a real mammogram of an average-sized breast was converted to a two-dimensional (2D) pixel value matrix. The pixel values in the raw image were given values of corresponding material thickness, using the inverse function of (1):

$$f^{-1}(p) = ap^b + c, \tag{2}$$

where p represents the pixel value.

In the third step, in order to achieve the best results, some de-noising and image resolution reduction had to take place. Here, the most important step is to take into account geometrical corrections for perspective and projection, as shown in Fig. 2.

X-ray image of the phantom was obtained at the distance of $f = 655$ mm between the focus and breast support plate.

Due to differences in the material thickness different attenuation will occur along the path of x-ray beam. However, one must take into account the divergence of the beam paths in order to achieve the exact correspondence of attenuation between real breast and 3D-printed phantom. The attenuation path lengths (z) in the phantom are calculated for each pixel of the image, assuming a parallel geometric projection. The

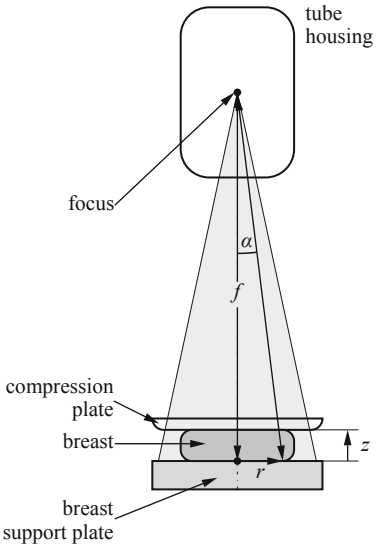

Fig. 2. Schematic representation of the imaging system with relevant geometrical parameters

corrections for divergence due to perspective was calculated using $z = 0$ and $z = f$ as coordinates of the breast support plate and focal point, respectively. To achieve this, following transformation needs to be used [12]:

$$\begin{bmatrix} x' \\ y' \\ z' \end{bmatrix} = \begin{bmatrix} M(z)x \\ M(z)y \\ \cos(\alpha)z \end{bmatrix} \tag{3}$$

with

$$M(z) = 1 - \frac{z}{f}, \quad \sin(\alpha) = \frac{r}{\sqrt{r^2 + f^2}}, \quad r = \sqrt{x^2 + y^2}. \tag{4}$$

After the perspective transformation of the phantom, the surface was triangulated to produce an STL file for printing.

2.4 Testing the Performance of the Phantom

We evaluated the successful performance of the phantom by utilizing an indirect method, which involved comparing the clinical images to those produced using the phantom.

We used three different measures to evaluate the quality of the reconstructed phantom medical image: peak signal-to-noise ratio (PSNR), structural similarity index (SSIM), and Pearson correlation coefficient (PCC). PSNR is a widely-used metric that measures the ratio of the maximum possible power of a signal to the power of corrupting noise [13, 14]. SSIM is a commonly used metric that assesses the visual quality of an image by comparing its structure to that of a reference image [15]. PCC is a statistical measure

that evaluates the linear relationship between two variables [16]. Also, we used the modulation transfer function (MTF) and noise power spectrum (NPS) to evaluate the overall quality of clinical and phantom images.

MTF and NPS are used to characterize the sharpness/resolution and noise of the imaging system. We obtained two medical images, the first one by imaging the patient and the second one by imaging a 3D phantom created from the original image. Using ImageJ software and the same calcification, we extracted data across the line of length 10 mm from both images with a pixel spacing of 0.07 mm which corresponds to detector size of 0.065 mm. We used a Gaussian normal distribution as a line spread function (LSF) to fit the extracted data

$$\mathrm{LSF}(x) = \frac{K}{2}\frac{1}{\sigma\sqrt{2\pi}}\exp\left(-\frac{(x-\mu)^2}{2\sigma^2}\right), \tag{5}$$

where K is a scaling factor.

From the parameters specified in the previous equation, we calculated the full width at half maximum (FWHM) of the LSF using the well-known formula $\mathrm{FWHM} = 2\sigma\sqrt{2\log 2}$ [17].

The relation between the LSF and MTF highlights the importance of understanding the system response for accurately characterizing the resolution of medical images [18, 19]. MTF can be determined from the LSF by using the absolute value of its Fourier transform. The analytical form of the MTF is

$$\mathrm{MTF}(f) = \frac{K}{2}\frac{1}{\sqrt{2\pi}}\exp\left(-\frac{f^2\sigma^2}{2}\right), \tag{6}$$

where f is the spatial frequency. Normalized function $\mathrm{MTF}_0(f)$ associated to $\mathrm{MTF}(f)$ such that $\mathrm{MTF}_0(0) = 1$ can be obtained by scaling. By Eq. (6) for a given value of MTF_0 we are able to determine corresponding spatial frequency. For the given $m \in (0, 1)$ from the equation $\mathrm{MTF}_0(f_m) = m$, follows that

$$f_m = \frac{\sqrt{-2\log m}}{\sigma}. \tag{7}$$

Another quantity used to characterize the images was the noise power spectrum (NPS), which is a widely used method for quantifying noise characteristics in digital imaging systems. The NPS analysis provided us with an estimate of the magnitude of noise at different spatial frequencies [20]. The formula used for the calculation is

$$\mathrm{NPS}(f_x, f_y) = \frac{1}{N}\sum_{k=1}^{N}\left|\mathrm{DF}_2(I_k(x,y) - \bar{I}_k)\right|^2\frac{\mathrm{d}x\mathrm{d}y}{N_x N_y}, \tag{8}$$

where DF_2 is 2D discrete Fourier transform, N is the number of regions of interest (ROIs), N_x and N_y are the number of pixels, and dx and dy are the pixel spacing along the x and y axis, respectively. In addition, $I_k(x, y)$ and $\bar{I}_k$ are the pixel intensities and average pixel intensity for the kth ROI, respectively [21].

From 2D NPS, 1D NPS can be calculated. Firstly, radial NPS is calculated by averaging over all spatial frequencies f_x and f_y with

$$f_r = \sqrt{f_x^2 + f_y^2}. \tag{9}$$

The range for both f_x and f_y is $[-f_N, f_N]$, where $f_N = 7.664\ \text{mm}^{-1}$ is the Nyquist frequency of pixel sampling. The final 1D NPS is the logarithm of obtained radial NPS. This curve represents the distribution of noise power as a function of the radial frequency f_r, and can be used to evaluate the noise characteristics of the imaging system.

3 Results and Discussion

A sample of the raw CC mammographic image was converted into a mesh object using MATLAB software. The grid object is printed using an SLA printer and the final phantom was imaged in an x-ray imaging system. A qualitative comparison of the original and final image shows that the process successfully transferred the anatomical information of the breast.

The two largest microcalcifications are clearly seen in the phantom image, and the contrast is similar to the contrast seen in the original image (Fig. 3). These microcalcifications can be readily seen in the printed object as tall columns extending above the shorter background columns. The results show that SLA technology can preserve very fine details on the phantom.

Different methods were used to quantify the quality of the clinical and phantom images. Table 1 shows the values of metrics (PSNR, SSIM, PCC) for the original phantom image (image 0) and cropped phantom image areas (images 1–3) compared to the originals. The PSNR values for the cropped images are higher than the PSNR value for the original image. The SSIM values for all images are close to 1. Finally, the PCC values show a strong linear relationship between the original image and the phantom image. We obtained slightly higher values of PCC for 1 and 3 than for image 2.

These results suggest that the cropped images are very similar to the original images, as indicated by the high SSIM values. This high-level similarity is almost the same for different pixel ranges of the images. The higher PSNR values for the cropped images further support this conclusion. The strong linear relationship between the original medical image and the cropped images, as indicated by the high PCC values, suggests that the phantom image is a good approximation of the original image.

Also, we obtained the parameters of the LSF were for the patient's original image ($\sigma = 0.558555$, $K = 350.152$, $\mu = 5.12341$) and for the phantom image ($\sigma = 0.56475$, $K = 377.438$, $\mu = 5.12638$) using the line over the microcalcification, as shown in Fig. 4A. For the corresponding values of the standard deviation, we obtained FWHM values of 1.330 mm and 1.315 mm for the phantom and patient images, respectively. The slightly smaller FWHM for the patient image indicates a better resolution compared to the phantom image.

For the commonly used value for medical images $m = 0.1$ and calculated values of σ, we obtained resolutions $3.800\ \text{mm}^{-1}$ and $3.842\ \text{mm}^{-1}$ for the phantom and patient images, respectively. This is clearly indicated in Fig. 5. Overall, our results indicate that

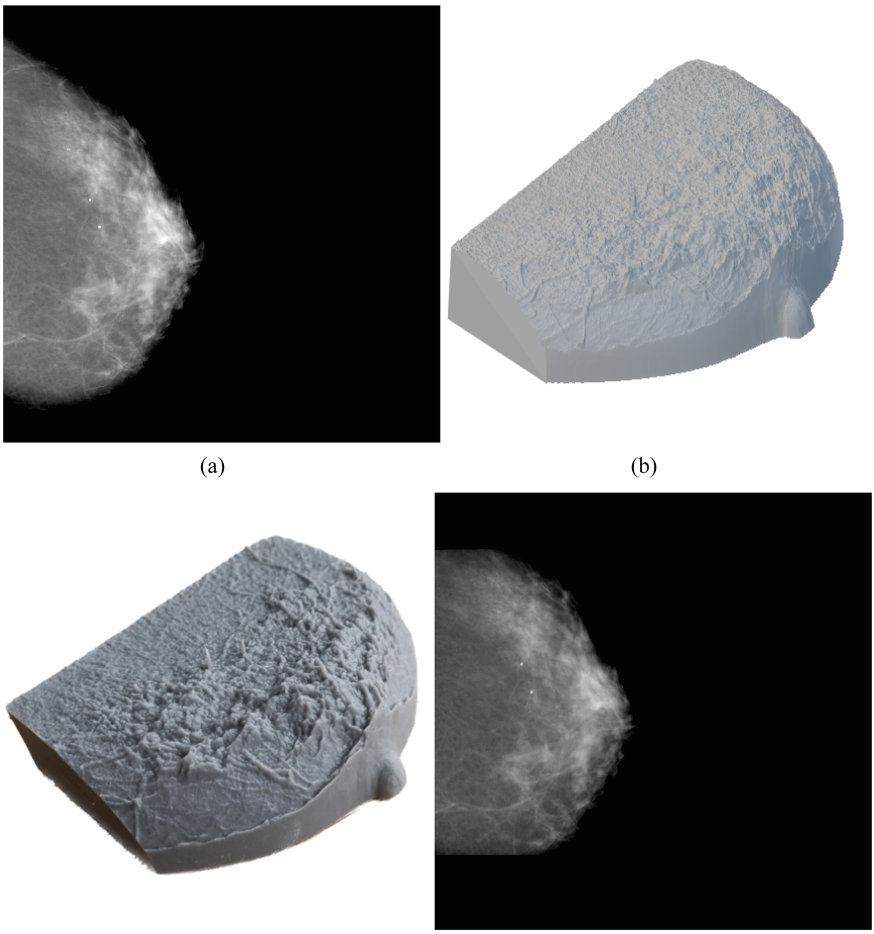

Fig. 3. Process of phantom manufacture: (a) Raw DICOM mammography image, (a) generated STL file, (c) 3D-printed phantom, (d) Raw DICOM phantom image

Table 1. Evaluation metrics for comparing the phantom image with the original patient image for different sizes

Image	PSNR	SSIM	PCC	x range	y range
0	46.2495	0.9893	0.9598	[0, 1500]	[0, 1500]
1	59.5757	0.9948	0.8990	[0, 1000]	[200, 1200]
2	59.4286	0.9947	0.8502	[0, 800]	[100, 1400]
3	59.6697	0.9949	0.8955	[100, 1000]	[100, 1300]

the patient image has a better resolution and higher spatial frequency compared to the phantom image.

We calculated the NPS using the analytical formula (8). Figure 4B indicates $N = 100$ ROIs, with $N_x \times N_y = 50 \times 50$. The chosen ROIs were relatively homogeneous, with no microcalcifications or high-density tissues. Figure 6 shows the logarithm of the NPS(f_r) plotted against radial frequency f_r. The results were analyzed to characterize the noise properties of the images.

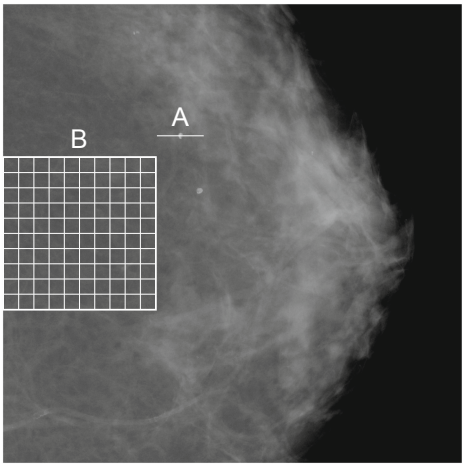

Fig. 4. Regions of interest used for evaluation of: (A) Modulation transfer function at a microcalcification, (B) Noise power spectrum in a relatively homogeneous part of the image.

Notably, the NPS curves for both the patient and phantom images are very similar. Some differences between two NPS curves can be observed at higher frequencies. They are caused by differences in quantum noise due to different detector air kerma $K_{\mathrm{i,d}}$ and could be corrected with the introduction of a scaling factor. However, the qualitative features of both curves (general shape and local maxima) are very similar, which indicates the same structural noise, which indicates a good overall similarity between two evaluated images.

4 Conclusions

The SLA 3D printing technology can be successfully utilized to produce mammography phantoms. The quality of the printed phantom was evaluated by comparing its images to those of the real patient mammogram using different quantifying measures in the spatial and frequency domain. The calculated SSIM was approximately 0.99, PSNR above 45, and PCC above 0.85. The resolution of the two images was similar, with values of 3.800 mm^{-1} and 3.842 mm^{-1} for the phantom and patient images, respectively. NPS curves for both the patient and phantom images are very similar, indicating the same structural noise. Some compromises had to be made in the reproduction of very

small objects due to the limiting resolution of the available SLA printers. The methods described in this study allow the manufacturing of anthropomorphic phantoms for only a fraction of the cost of similar commercially available phantoms, as well as the production of patient-specific phantoms that could be used for different purposes in medicine.

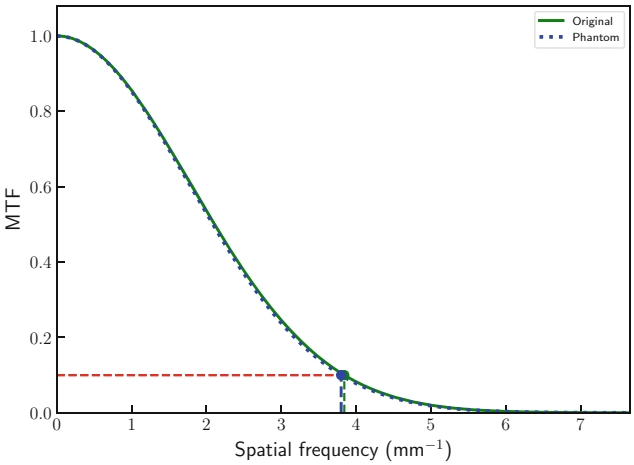

Fig. 5. MTF curve for patient's and phantom's image. The dashed lines indicate values of spatial frequency at MTF $= 0.1$ for both images.

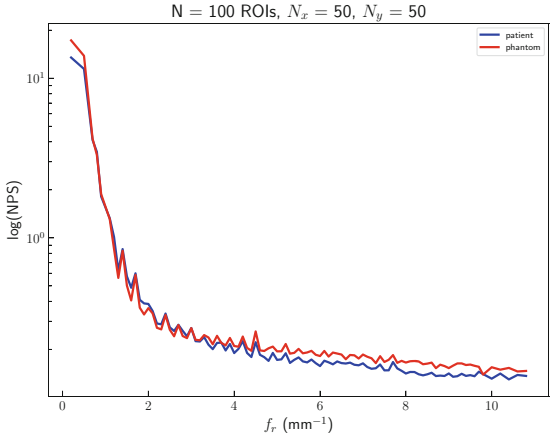

Fig. 6. The 1D NPS plot presented in logarithmic scale for original and phantom images with resolution 50×50 pixels and 100 ROIs as shown in Fig. 4.

References

1. Bosmans, H., et al.: Radiat. Prot. Dosimetry **117**(1–3), 120 (2005)
2. Bouwman, R.W., et al.: Med. Phys. **44**(11), 5726 (2017)
3. Cockmartin, L., et al.: Phys. Med. Biol. **62**(3), 758 (2017)
4. Balta, C., et al.: Med. Phys. **45**(2), 655 (2018)
5. Schopphoven, S., Cavael, P., Bock, K., Fiebich, M., Mäder, U.: Phys. Med. Biol. **64**(21), 215005 (2019)
6. Markey, M.K.: Physics of Mammographic Imaging. CRC Press (2012)
7. DeWerd, L.A., Kissick, M.: The Phantoms of Medical and Health Physics. Springer (2014)
8. Martin, C., Sharp, P., Sutton, D.: Appl. Radiat. Isot. **50**(1), 21 (1999)
9. Badal, A., Clark, M., Ghammraoui, B.: J. Med. Imaging **5**(3), 033501 (2018)
10. Pandzic, A.: Group (Fig. 1) **4**(5), 6 (2021)
11. Pizzolato, N., et al.: J. Phys. Conf. Ser. **1512**, 012038 (IOP Publishing, 2020)
12. Irnstorfer, N., Unger, E., Hojreh, A., Homolka, P.: Sci. Rep. **9**(1), 14357 (2019)
13. Szeliski, R.: Computer Vision: Algorithms and Applications. Springer Nature (2022)
14. Hore, A., Ziou, D.: In: 2010 20th International Conference On Pattern Recognition, pp. 2366–2369. IEEE (2010)
15. Sampat, M.P., Wang, Z., Gupta, S., Bovik, A.C., Markey, M.K.: IEEE Trans. Image Process. **18**(11), 2385 (2009)
16. Neto, A.M., Victorino, A.C., Fantoni, I., Zampieri, D.E., Ferreira, J.V., Lima, D.A.: In: 2013 13th International Conference on Autonomous Robot Systems, pp. 1–6. IEEE (2013)
17. Ekström, P.: Statistics and the Treatment of Experimental Data. Lunds universitet (1996)
18. Kao, Y.H., Albert, M., Carton, A.K., Bosmans, H., Maidment, A.D.: In: Medical Imaging 2005: Physics of Medical Imaging, vol. 5745, pp. 1199–1208. SPIE (2005)
19. Manzanares, A., Calvo, M., Chevalier, M., Lakshminarayanan, V.: Appl. Opt. **36**(19), 4362 (1997)
20. Park, H.S., Kim, H.J., Cho, H.M., Jung, J., Lee, C.L.: In: 2008 IEEE Nuclear Science Symposium Conference Record, pp. 4378–4383. IEEE (2008)
21. Dolly, S., Chen, H.C., Anastasio, M., Mutic, S., Li, H.: J. Appl. Clin. Med. Phys. **17**(3), 392 (2016)